Supporting Information

Panpan Chang,[ab] Kazuki Matsumura,[c] Jizong Zhang,[ab] Jie Qi,[ab] Chengyang Wang,[ab] Taro Kinumoto,[c] Tomoki Tsumura,[c] Mingming Chen,[*abc] and Masahiro Toyoda[*c]

[a] Key Laboratory for Green Chemical Technology of MOE, School of Chemical Engineering and Technology, Tianjin University, Tianjin 300350, P. R. China

[b] Collaborative Innovation Center of Chemical Science and Engineering (Tianjin), Tianjin University, Tianjin 300350, P. R. China

[c] Department of Applied Chemistry, Faculty of Engineering, Oita University, 700 Dannoharu, Oita 870-1192, Japan

1. Structural Characterization

Powder X-ray diffraction (XRD) pattern was conducted on Rigaku D/Max 2500 v/PC system using Cu Kα radiation (40 kV, λ=1.54051 Å). Thermal gravimetric analysis (TG) was performed on a TA-50 system at 5 °C·min^{-1} under N_2 atmosphere. Elemental analysis was conducted by a Vario EL Ⅲ elemental analyzer, by which C, H, N, S and O contents of samples can be obtained directly. The Fourier transform infrared spectroscopy (FT-IR) of samples was characterized using a Nicolet Magna-560 FT-IR spectrometer with wavenumber range from 400 to 4000 cm^{-1}. X-ray photoelectron spectroscopy (XPS) analysis was carried on a PHI-1600 ESCA electron system using Al Kα (1486.6 eV) radiation to get the surface atomic components.

2. Electrochemical measurements

The electrochemical measurements in this work used the most reliable industrial test method raised by Gogotsi's group to ensure credible data [1, 2]. This method requires two key points: (1) the electrode thickness should be in the range of 100 to 200 μm; (2) the measurement should use the two-electrode symmetrical system instead of the three-electrode system.

Following the aforementioned principles, in our work, the electrode diameter and the electrode thickness were respectively 1.3 cm and 120 μm. The active material mass of PCN5 and PCN6 electrode were respectively 7.7 and 5.8 mg. Thus the areal loading mass of PCN5 and PCN6 electrode were respectively 5.8 and 4.37 mg cm^{-2}; while the densities (ρ) of PCN5 and PCN6 electrode were respectively 0.483 and 0.364 g cm^{-3}.

The gravimetric specific capacitance (C_g), the volumetric specific capacitance (C_v), the gravimetric energy density (E_g), the average gravimetric power density (P_g), the volumetric energy density (E_v), the average volumetric power density (P_v) were obtained by the following formula [1]:

$$dV/dt = (V_{max}-V_{1/2max})/(t_{1/2max}-t_{max}) \quad (1)$$

$$C = I/(dV/dt) \quad (2)$$

$$C_g = 4C/m \quad (3)$$

$$C_v = \rho * C_g \quad (4)$$

$E_g = 1/8*C_g*V^2$ (5)

$P_g = 3600*E_g/t_{max}$ (6)

$E_v = 1/8*C_v*V^2$ (7)

$P_v = 3600*E_v/t_{max}$ (8)

in which C is the capacitance (F) of total capacitor and C_g is the gravimetric specific capacitance (F g^{-1}) towards the active material in one electrode, I is the current (A), m is the total active material mass (g) in a device, V_{max} and t_{max} stand for the maximum discharge voltage (V) and corresponding time (s), $V_{1/2max}$ and $t_{1/2max}$ stand for the half of maximum discharge voltage (V) and corresponding time (s), V represents the operating voltage (V, subtracting V_{drop} from V_{max}), C_v is the volumetric specific capacitance (F cm^{-3}) towards the active material in one electrode, E_g and P_g are respectively the gravimetric energy density (Wh kg^{-1}) and average gravimetric power density (W kg^{-1}) of the total capacitor, E_v and P_v are respectively the volumetric energy density (Wh L^{-1}) and average volumetric power density (W L^{-1}) of the total capacitor.

3. XRD spectrum of raw material SP

XRD spectrum of raw material SP is exhibited in Fig. S1. Two peaks at 25.9° and 42.5° are respectively attributed to (002) peak and (100) peak of carbon materials. The average microcrystalline size of sp^2 carbon domains in SP was calculated from the XRD spectrum (Table S1). The calculated crystal size L_c is 1.87 nm and the planar aromatic size L_a is 3.2 nm, illustrating that the sp^2 carbon domains in SP have few stacking layers and ultra-small polyaromatic hydrocarbons.

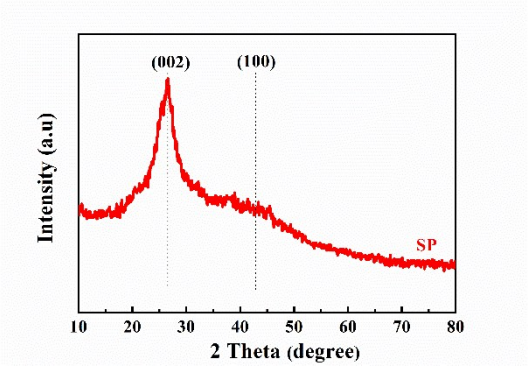

Fig. S1. XRD spectrum of SP.

Table S1 XRD parameters of SP

Sample	$2\theta_{002}$/°	d_{002}/nm	L_c/nm	$2\theta_{100}$/°	L_a/nm
SP	25.9	0.3437	1.87	42.5	3.2

4. The physical properties of raw material SP and F127

Raw material SP (Table S2) mainly contains C, O atoms and slight amount of heteroatoms such as H, N and S atoms. Ample oxygen-containing groups exist in the FT-IR spectrum of SP (Fig. S2). These oxygen-containing groups contain phenol, alcoholic hydroxyl, carbonyl, carboxyl, ether, lactone and quinone, which is consistent with TPD results (Fig. 1a&b). In addition, some oxygen-containing groups also exist in the form of -SO_3H in SP. All the oxygen configurations furnish SP completely soluble

in water.

Table S2 Elemental analysis and surface atom analysis of SP

Sample	Elemental analysis (*wt*/%)					Surface atom analysis (*at*/%)				
	C	N	H	S	O	C	N	S	O	C/O
SP	43.87	0.79	2.75	1.3	51.29	74.8	1.5	0.4	23.3	3.21

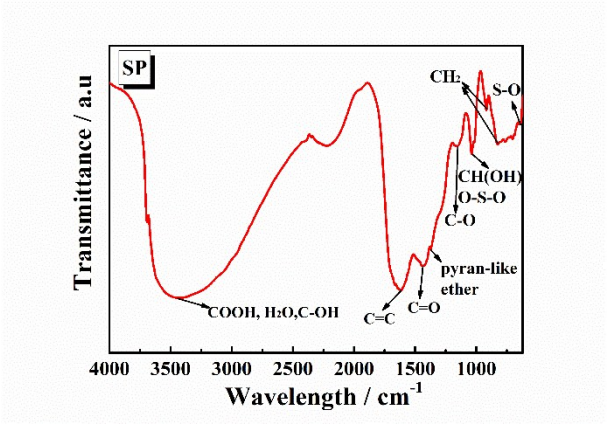

Fig. S2. FT-IR spectrum of SP

C 1s and O 1s XPS spectra of SP (Fig. S3) explicitly expound the chemical state of C and O atoms. In Fig. S3a, the C 1s peak at 284.6 eV stands for the dominant sp^2-bonding carbons (polyaromatic hydrocarbon) in SP; while the C 1s peak at 285.3 eV represents the sp^3-bonding carbons, illustrating the existence of a certain amount of aliphatic hydrocarbon in SP. At higher binding energy, three weaker peaks respectively stand for -C-O group (at 286.4 eV), -C=O group (at 288 eV) and -COOH group or π-π^* transition (at 289 eV) [3], proved by O 1s spectrum in Fig. S3b. Three peaks at 531.1 eV, 532.3 eV and 533.7 eV can be respectively classified as: -C=O group in the form of carbonyl, lactone, anhydride or quinone; -C-O group in the form of ether, alcoholic hydroxyl or phenol; and -COOH group [4]. More importantly, the oxygen-containing groups in SP are mainly in the form of -C=O group and -C-O group (with total contents of 95.7%), rather than -COOH group (with content of only 4.3%). The surface atom analysis of SP was summarized in Table S2. The atomic percentages of C, O, N, S atoms in SP are respectively 74.8%, 23.3%, 1.5% and 0.4%. Considering the elemental and XPS analysis together, it can be concluded that the oxygen-containing groups in SP are not only on the material surface but also within the materials.

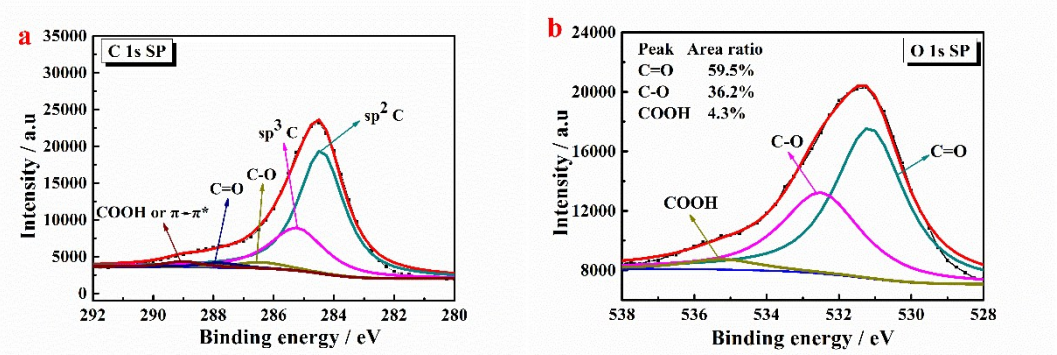

Fig. S3. C 1s (a) and O 1s (b) XPS spectra of SP

TG&DTG curves (Fig. S4) shows that during the heat-treatment, F127 molecules can absolutely decompose below 410 °C. And the weight loss rate of F127 molecules reaches up to the maximum at 386 °C.

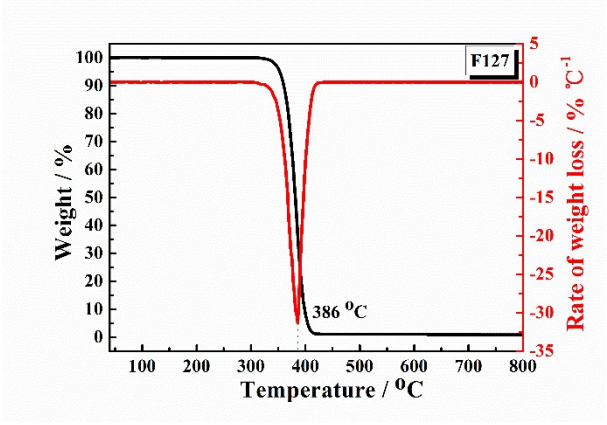

Fig. S4. TG&DTG curves of F127

5. TPD resolving of SP

Table S3 summarizes the oxygen-containing functional groups in SP resolving from TPD spectra (Fig. 1a&b). Raw material SP has different kinds of functional groups such as carboxyl, lactone, anhydride, phenol, carbonyl and quinone.

Table S3 TPD resolving results of SP

Sample	CO				CO_2			
	Peak	Location/°C	Amount/ (μmol g^{-1})	Functional group	Peak	Location/°C	Amount/ (μmol g^{-1})	Functional group
SP	1	577	48.1	Anhydride+ phenol	1	390	746.5	Carboxyl
	2	600	15		3	640	260	Anhydride
	3	650	500		2	498	1480	
	4	737	52.9	Carbonyl	4	733	398.1	Lactone
	5	860	1829.5					
	6	1047	91.7	Quinone				
	7	1090	104					

6. HR-TEM image of SP

HR-TEM image of PCN6 in Fig. S5 give convictive evidence about the mesopores with size range of 2-7 nm (indicated by the red circles), which is highly consistent with the pore size distribution of PCN6 in Fig. 4b.

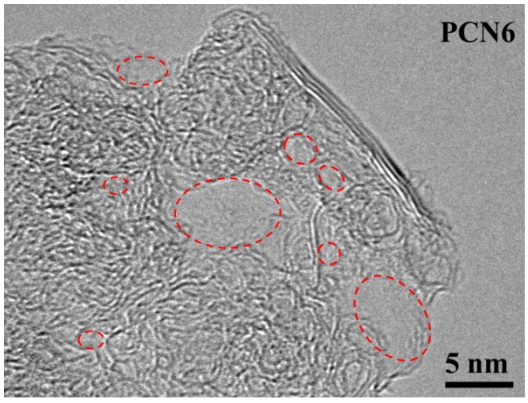

Fig. S5. HR-TEM image of PCN6.

7. XPS and elemental analysis of PCNs

Elemental analysis and surface atom analysis of PCNs were given in Table S4. After activation, the C contents of PCNs increase evidently and the O contents of PCNs declines obviously, implying the removal of most unstable oxygen-containing groups. Furthermore, the O atoms in PCNs cannot be fully eliminated. The O contents of PCN5 and PCN6 are respectively 8.27*wt*% and 7.86*wt*%. It is understandable because TG and TPD results clearly prove that the stable carbonyl and quinone groups can still exist even after 850 °C heat-treatment.

Table S4 Elemental analysis and surface atom analysis of PCNs.

Sample	Elemental analysis (*wt*/%)					Surface atom analysis (*at*/%)				
	C	N	H	S	O	C	N	S	O	C/O
PCN5	89.33	0.65	0.87	0.88	8.27	88.6	1.3	0.3	9.8	9.04
PCN6	90.02	0.62	0.7	0.8	7.86	90.6	1.3	0.2	7.9	11.47

C 1s and O 1s spectra of PCNs (Fig. S6) afford detailed information about the chemical state of C and O atoms. PCNs are composed of dominant sp^2-bonding carbons (at 284.6 eV), moderate sp^3-bonding carbons (at 285.3 eV) and slight carbon atoms in the form of oxygen-containing groups. After activation, O 1s peaks of PCNs decrease remarkably. According to the TG and TPD results, three peaks at 531.1 eV, 532.3 eV and 533.7 eV are respectively assigned to -C=O group in carbonyl or quinone, -C-O group in ether and -COOH, in which -C-O group is predominant [5]. Furthermore, because of more drastic activation, PCN6 has less O content than PCN5.

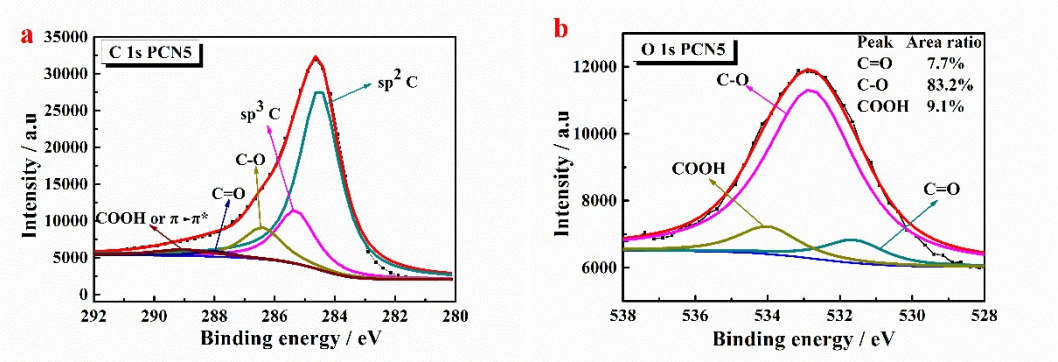

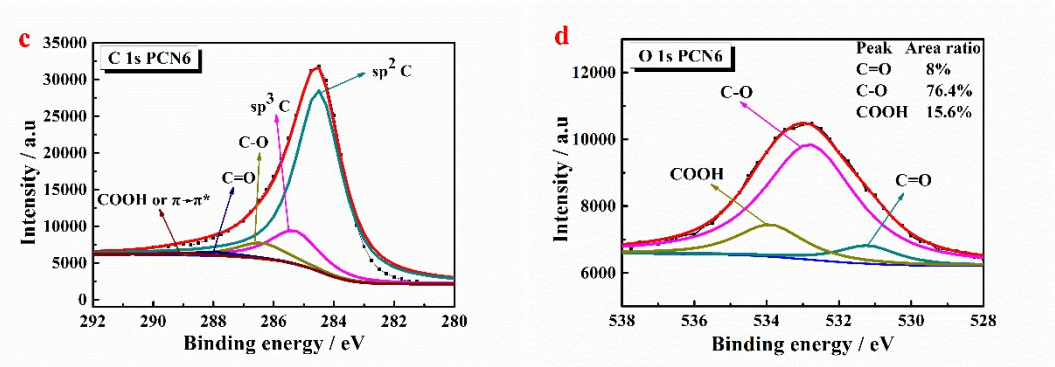

Fig. S6. C 1s (a, c) and O 1s (b, d) XPS spectra of PCN5 (a, b) and PCN6 (c, d).

8. Performance of PCNs and reported EDLC electrode materials in organic electrolyte and ionic liquid electrolyte in literature.

Table S5 Performances of PCNs and reported EDLC electrode materials in organic electrolyte (1 M $TEABF_4$ using PC or AN as solvent, or $NaClO_4$ using EC and DMC as solvent) and ionic liquid electrolyte.

Sample	Gravimetric capacitance			Cycle performance			Ragone plots		Remarks
	Current density (A g^{-1})	Voltage (V)	C_g (F g^{-1})	Current density (A g^{-1})	Cycles	Capacitance retention (%)	E_g (Wh kg^{-1})	P_g (kW kg^{-1})	
PCN5	**10**	**2.7**	**128**	**2.5**	**10^4**	**84.8**	**31.1**	**13.5**	**PCN ($TEABF_4$/PC)**
PCN6	**10**	**2.7**	**143**	**2.5**	**10^4**	**90.8**	**34.1**	**13.5**	**PCN ($TEABF_4$/PC)**
CK-850 [6]	10	2	132	10	10^4	92	20	9.5	PCN ($TEABF_4$/AN)
PCNS-G-4 [7]	10	2.5	100		-		10.3	18.4	PCN ($TEABF_4$/AN)
GNa-CA [8]	10	2.7	115	10	10^4	87	27	15	PCN ($TEABF_4$/AN)
aPG-10 [9]	10	3.5	70		-		29.8	6.75	Graphene ($TEABF_4$/AN)
F310-800 [5]	10	3	92	2.5	10^4	82.1	28.8	7.5	C/C composite ($TEABF_4$/PC)
C-700 [10]	10	2.5	60		-		12	13.5	PCN ($TEABF_4$/AN)
NMCS-3-A [11]	10	2	90		-		12.5	6.75	Porous carbon sphere ($TEABF_4$/AN)
CDC-1 [12]	8	3	96	4	10^4	94	28	6	Biomass-derived carbon ($NaClO_4$/EC-DMC)
C800 [13]	10	2.5	135	5	10^4	90.3	31	0.31	HPC ($TEABF_4$/AN)
A1G [14]	10	2.7	157	1	$8*10^3$	89	30	13.5	HPC ($TEABF_4$/AN)
CDC-Aero-700 [15]	10	2	98		-		13.6	5.8	Carbide-derived carbon aerogels ($TEABF_4$/AN)
PCN5	**10**	**3.5**	**91**	**2.5**	**10^4**	**75.4**	**35.3**	**17.5**	**PCN ($EMIMBF_4$)**
PCN6	**10**	**3.5**	**163**	**2.5**	**10^4**	**86.6**	**67.1**	**17.5**	**PCN ($EMIMBF_4$)**
HPNC-NS [16]	10	3.5	155	2	10^4	92	52.5	8.75	N-doped PCN ($EMIMBF_4$)
BHNC [4]	10	3.5	112	1	$5*10^3$	95	44	17.5	HPC (EMIMTFSI)

F310-800 [5]	10	3.5	95	2.5	$5*10^3$	91.9	40.5	8.75	C/C composite ($EMIMBF_4$)
NMCS-3-A [11]	10	3	80		-		25	8.75	Porous carbon sphere ($EMIMBF_4$)
PCF-900 [17]	10	3.5	187	5	$5*10^3$	88	66	6.8	PCN ($EMIMBF_4$)
GPC [18]	10	3.5	117	2	10^3	89.5	34	17.5	HPC (EMIMTFSI)
PGBC-1 [19]	10	3	50	1	$5*10^3$	95	18	15	Porous graphitic biomass carbon (EMIMTFSI)
CDC-Aero-700 [15]	10	3.5	140		-		59.5	8.75	Carbide-derived carbon aerogels ($EMIMBF_4$)

* All the capacitance is based on the mass of the active material on a single electrode

Table S6 Comparison of volumetric performances of PCNs and reported EDLC electrode materials in organic electrolyte (1 M $TEABF_4$ using PC or AN as solvent) and ionic liquid electrolyte.

Sample	Electrode density ($g\ cm^{-3}$)	Electrode thickness (μm)	Mass loading ($mg\ cm^{-2}$)	Electrolyte / Voltage (V) / Current density ($A\ g^{-1}$)	C_g ($F\ g^{-1}$)	C_v ($F\ cm^{-3}$)	E_g ($Wh\ kg^{-1}$) / P_g ($kW\ kg^{-1}$)	E_v ($Wh\ L^{-1}$) / P_v ($kW\ L^{-1}$)
PCN5	**0.483**	**120**	**5.8**	**$TEABF_4$-PC / 2.7 / 10**	**128**	**61.8**	**31.1 / 13.5**	**15 / 6.52**
PCN6	**0.364**	**120**	**4.37**	**$TEABF_4$-PC / 2.7 / 10**	**143**	**52**	**34.1 / 13.5**	**12.4 / 4.9**
F310-800 [5]	0.41	200	8.21	$TEABF_4$-PC / 3 / 10	92	37.7	28.8 / 7.5	11.8 / 3.07
A1G [14]	0.35	100-120	3-4	$TEABF_4$-AN / 2.7 / 10	157	55.3	30 / 13.5	10.5 / 4.73
GNa-CA [8]	0.4	125	5	$TEABF_4$-AN / 2.7 / 10	115	46	27 / 15	10.8 / 6
PCNS-G-4 [7]	0.1	100	1	$TEABF_4$-AN / 2.5 / 10	100	10	10.3 / 18.4	1.03 / 1.84
CK-850 [6]	0.42	-	-	$TEABF_4$-AN / 2 / 10	132	55.5	16 / 9.5	6.72 / 4
aPG-10 [9]	0.72	40	2.88	$TEABF_4$-AN / 3.5 / 10	70	50.4	29.8 / 6.75	21.4 / 4.86
PF16G-HA [20 a]	0.4	100-120	4	$TEABF_4$-AN / 2.7 / 10	174	70	51 / 109	20 / 44
Compressed a-MEGO [21 a]	0.61	72	4.4	$TEABF_4$-AN / 2.7 / 1	122	74	31 / 52.4	19 / 32
a-MEGO [22 a]	0.36	40-50	1.44-1.8	$TEABF_4$-AN / 2.7 / 3.8	141	50.7	39 / 145	14 / 52.2

PCN5	**0.483**	**120**	**5.8**	**EMIMBF$_4$ / 3.5 / 10**	**91**	**44**	**35.3 / 17.5**	**17 / 8.45**
PCN6	**0.364**	**120**	**4.37**	**EMIMBF$_4$ / 3.5 / 10**	**163**	**59.3**	**67.1 / 17.5**	**24.4 / 6.37**
F310-800 [5]	0.41	200	8.21	EMIMBF$_4$ / 3.5 / 10	95	39	40.5 / 8.75	16.6 / 3.59
HPNC-NS [16]	0.467	128	6	EMIMBF$_4$ / 3.5 / 10	155	72.4	52.5 / 8.75	24.5 / 4.08
PCF-900 [17]	0.515	155	8	EMIMBF$_4$ / 3.5 / 10	187	96.3	66 / 6.8	34 / 3.5
aPG-10 [9 a]	0.72	40	2.88	BMIMPF$_6$-AN / 3.5 / 10	107	77	89 / 99	64 / 71.2
a-MEGO [22 a]	0.36	40-50	1.44-1.8	BMIMBF$_4$-AN / 3.5 / 5.7	166	60	70 / 250	25.2 / 90
Compressed a-MEGO [21 a]	0.61	72	4.4	BMIMBF$_4$-AN / 3.5 / 1.22	158	96	67 / 32.7	40.8 / 20
LSG [23 a]	0.048	7.6	0.036	EMIMBF$_4$ / 3.5 / 1	276	13.2	117.4 / 416	5.6 / 20
PF16G-HA [20 a]	0.4	100-120	4	EMIMBF$_4$ / 3.5 / 10	210	84	98 / 137	39 / 55

[a] The P_g value and P_v value in the references [9, 20-23] represent the maximum power density (P_{max}); and the P_g value and P_v value in our work and other references represent the average power density (P_{ave}).

"-": Not available.

9. Postmortem analyses of PCNs after cycling tests

The structural stability of the 2D porous nanosheets can largely affect the EDLC performances. Postmortem analyses of PCN5 and PCN6 in both $TEABF_4$/PC and pure $EMIMBF_4$ electrolytes after cycling tests were exhibited in Fig. S7. It can be seen that the thickness of PCN6 (Fig. S7b&d) was obviously thinner than that of PCN5 (Fig. S7a&c), coinciding with Fig. 2 in the manuscript. More importantly, the typical 2D architectures of PCNs after cycling tests can be well preserved in both electrolytes (Fig. S7). And there are not any cracks in the micron-sized 2D nanosheets. It illustrates that PCNs have good structural stability, which benefits from the chemical covalent-bond connections among the graphitic microcrystallines in PCNs. The rigid structures can furnish PCNs excellent energy storage features in the whole cycling life [24].

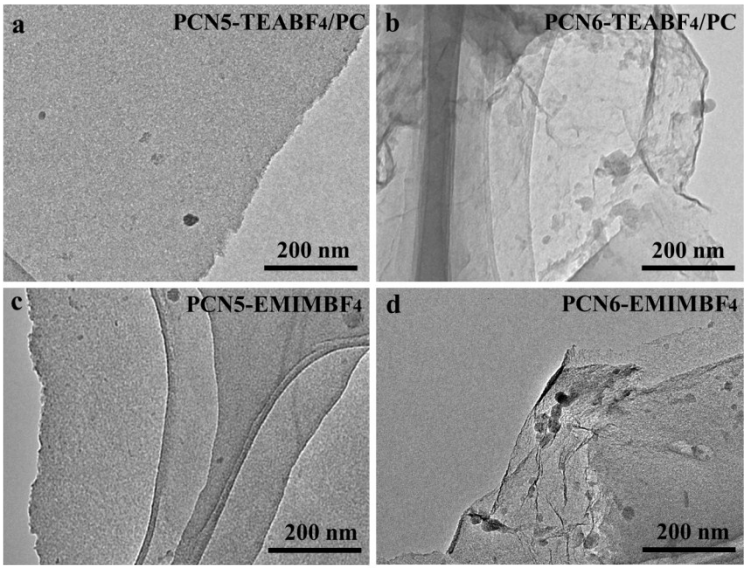

Fig. S7. Postmortem analyses of PCN5 and PCN6 after cycling tests. TEM images of PCN5 (a) and PCN6 (b) in 1 M $TEABF_4$/PC electrolyte after 10,000 cycles; TEM images of PCN5 (c) and PCN6 (d) in pure $EMIMBF_4$ electrolyte after 10,000 cycles.

References

1. M. D. Stoller and R. S. Ruoff, *Energy & Environmental Science*, 2010, **3**, 1294-1301.
2. Y. Gogotsi and P. Simon, *Science*, 2011, **334**, 917-918.
3. I. K. Moon, J. Lee, R. S. Ruoff and H. Lee, *Nature communications*, 2010, **1**, 73.
4. W. Tian, Q. Gao, Y. Tan, K. Yang, L. Zhu, C. Yang and H. Zhang, *Journal of Materials Chemistry A*, 2015, **3**, 5656-5664.
5. P.-p. Chang, C.-y. Wang, T. Kinumoto, T. Tsumura, M.-m. Chen and M. Toyoda, *Carbon*, 2018.
6. M. Sevilla and A. B. Fuertes, *ACS nano*, 2014, **8**, 5069-5078.
7. X. Fan, C. Yu, J. Yang, Z. Ling, C. Hu, M. Zhang and J. Qiu, *Advanced Energy Materials*, 2015, **5**.
8. A. B. Fuertes and M. Sevilla, *ACS applied materials & interfaces*, 2015, **7**, 4344-4353.
9. J. Xu, Z. Tan, W. Zeng, G. Chen, S. Wu, Y. Zhao, K. Ni, Z. Tao, M. Ikram, H. Ji and Y. Zhu, *Adv Mater*, 2016, **28**, 5222-5228.
10. W. Yang, W. Yang, F. Ding, L. Sang, Z. Ma and G. Shao, *Carbon*, 2017, **111**, 419-427.
11. J. Tang, J. Wang, L. K. Shrestha, M. S. A. Hossain, Z. A. Alothman, Y. Yamauchi and K. Ariga, *ACS Appl Mater Interfaces*, 2017, **9**, 18986-18993.
12. R. Thangavel, K. Kaliyappan, H. V. Ramasamy, X. Sun and Y. S. Lee, *ChemSusChem*, 2017, **10**, 2805-2815.
13. J. Yang, H. Wu, M. Zhu, W. Ren, Y. Lin, H. Chen and F. Pan, *Nano Energy*, 2017, **33**, 453-461.
14. M. Zhang, Z. Sun, T. Zhang, B. Qin, D. Sui, Y. Xie, Y. Ma and Y. Chen, *Journal of Materials Chemistry A*, 2017, **5**, 21757-21764.
15. M. Oschatz, S. Boukhalfa, W. Nickel, J. P. Hofmann, C. Fischer, G. Yushin and S. Kaskel, *Carbon*, 2017, **113**, 283-291.

16. J. Hou, C. Cao, F. Idrees and X. Ma, *ACS nano*, 2015, **9**, 2556-2564.
17. J. Hou, K. Jiang, R. Wei, M. Tahir, X. Wu, M. Shen, X. Wang and C. Cao, *ACS applied materials & interfaces*, 2017, **9**, 30626-30634.
18. X.-F. Hao, Y. Yan, L.-G. Gao, W.-S. Mu and C. Hao, *Electrochimica Acta*, 2017, **241**, 124-131.
19. Y. Gong, D. Li, C. Luo, Q. Fu and C. Pan, *Green Chemistry*, 2017, **19**, 4132-4140.
20. L. Zhang, F. Zhang, X. Yang, G. Long, Y. Wu, T. Zhang, K. Leng, Y. Huang, Y. Ma and A. Yu, *Scientific reports*, 2013, **3**.
21. S. Murali, N. Quarles, L. L. Zhang, J. R. Potts, Z. Tan, Y. Lu, Y. Zhu and R. S. Ruoff, *Nano Energy*, 2013, **2**, 764-768.
22. Y. Zhu, S. Murali, M. D. Stoller, K. Ganesh, W. Cai, P. J. Ferreira, A. Pirkle, R. M. Wallace, K. A. Cychosz and M. Thommes, *science*, 2011, **332**, 1537-1541.
23. M. F. El-Kady, V. Strong, S. Dubin and R. B. Kaner, *Science*, 2012, **335**, 1326-1330.
24. Y. Liu, X.-Y. Yu, Y. Fang, X. Zhu, J. Bao, X. Zhou and X. W. Lou, *Joule*, 2018, DOI: 10.1016/j.joule.2018.01.004.